
Towards cross-platform automated rotation electron diffraction

Authors

Maria Roslova^a, Stef Smeets^b, Bin Wang^a, Thomas Thersleff^a, Hongyi Xu^a and Xiaodong Zou^{a*}

^aDepartment of Materials and Environmental Chemistry (MMK), Stockholm University, Svante Arrhenius väg 16C, Stockholm, SE-10691, Sweden

^bDepartment of Bionanoscience, Kavli Institute of Nanoscience, Delft University of Technology, Van der Maasweg 9, Delft, HZ-2629, Netherlands Antilles

Correspondence email: x.zou@mmk.su.se

Synopsis A DigitalMicrograph script was developed to coordinate TEM goniometer rotation and detector image recording for continuous rotational electron diffraction (cRED) data acquisition. Exploiting fast, automated data collection, it was revealed how experimental settings (selected area mode illumination, parallel nanoprobe mode illumination and different electron dose rate) affect the quality of cRED data.

Abstract A DigitalMicrograph script *InsteaDMatic* has been developed to facilitate rapid automated continuous rotation electron diffraction (cRED) data acquisition. The script coordinates microscope functions such as stage rotation and camera functions relevant for data collection, and stores the experiment metadata. The script is compatible with both JEOL and Thermo Fisher Scientific microscopes. A proof-of-concept has been performed through employing *InsteaDMatic* for data collection and structure determination of a ZSM-5 zeolite. The influence of illumination settings and electron dose rate on the quality of diffraction data, unit cell determination and structure solution has been investigated in order to optimize the data acquisition procedure.

Keywords: 3D electron diffraction, DigitalMicrograph script, automated data collection, structure determination, microED

1. Introduction

3D electron diffraction (3D ED) is a well-known technique for structure determination of solids, which is especially advantageous for studies of micro- and nanocrystals. So far, 3D ED data have been used for determination of more than 200 structures (Gemmi *et al.*, 2019), such as zeolites (Jiang *et al.*, 2011; Guo *et al.*, 2015; Simancas *et al.*, 2016; Lee *et al.*, 2018; Bieseki *et al.*, 2018; Zhang *et al.*, 2018), metal-organic frameworks (Denysenko *et al.*, 2011; Feyand *et al.*, 2012; Wang, Rhauderwiek *et al.*, 2018; Lenzen *et al.*, 2019), pharmaceuticals (van Genderen *et al.*, 2018; Brázda *et*

al., 2019), and protein crystals (Nannenga *et al.*, 2014; de la Cruz *et al.*, 2017; Xu *et al.*, 2019) and many others. 3D ED data is traditionally collected by stepwise tilting a crystal around an arbitrary tilt axis within the full tilt range of the microscope goniometer and recording a set of diffraction patterns (Kolb *et al.*, 2007; Nannenga *et al.*, 2014; Zhang *et al.*, 2010). Examples of software which is able to perform crystal tilt, crystal position tracking and diffraction pattern acquisition are described in (Kolb *et al.*, 2007; Wan *et al.*, 2013; Zhang *et al.*, 2010; Wan *et al.*, 2013). A perspective approach to 3D ED, known as MicroED (Nannenga *et al.*, 2014) or cRED, is based on a continuous data collection while the goniometer is rotating. Automation of cRED data collection helps to reduce large number of manual operations and to obtain reproducible results with less human efforts, especially for very large datasets. Up to date, a limited number of software packages are available, designed to interface with both the camera and the microscope and collect multiple diffraction patterns, and those are often commercial and closed source, e.g. *iTEM* software from Olympus Soft Imaging Solutions GmbH, Münster, Germany (Gemmi *et al.*, 2015). Recently, a script has been developed for an open-source, widely-used in the cryo-electron microscopy community *SerialEM* software enabling large-scale MicroED data collection on Thermo Fisher Scientific (TFS) microscopes with electron detectors from various manufacturers (de la Cruz *et al.*, 2019). In our lab for cRED data collection we developed *Instamatic*, a custom software designed for electron crystallography needs, which is able to control both microscope and camera (Smeets *et al.*, 2018), and affords additional features such as crystal tracking through defocusing of diffraction pattern (Cichocka *et al.*, 2018; Wang *et al.*, 2019).

However, to the best of our knowledge, currently there is no widely applicable routine to collect 3D ED data using continuous rotation, and particularly there is no widely accessible and easy-to-install software available. The desired software should neither have steep learning curves nor require its own set calibrations to be performed nor complicated set-ups. Due to diversity of existing TEM platforms the software has to control both the camera and the microscope, dealing with different combinations of those. Here, we propose to employ DigitalMicrograph (DM) (Digital Micrograph GATAN, Pleasanton, CA, U.S.A.) as a mediator controlling hardware interactions between microscope and camera. We developed a dedicated DM script for automated cRED data collection. The script, which we named *InsteaDMatic* was tested on our Themis Z (TFS) equipped with a Gatan OneView camera and JEM2100F (JEOL) with Gatan Orius SC200D camera. The script is successfully trialling now in five labs worldwide equipped with JEM2100F, JEM3100F and TFS Talos microscopes with different Gatan cameras. The *InsteaDMatic* follows the same data collection workflow as described previously (Cichocka *et al.*, 2018) but communicates to both the microscope and camera *via* DM interfaces. The benefit of this design philosophy is easiness of installation and enhanced transferability, since the DM software is an integral part of a vast majority of electron microscopy systems nowadays. To demonstrate the capability of the script, we collected high-quality data on a ZSM-5 zeolite with up to 0.80 Å resolution providing a solid basis for its structure solution. The data quality and the resulting

data statistics have been compared for crystals illuminated in selected area mode or in parallel nanoprobe mode. To highlight the advantages of the approach, parameters such as electron dose rate and monochromator focus have been tailored during the collection of RED data.

2. Experimental

2.1. Sample preparation

Thoroughly ground ZSM-5 aluminosilicate zeolite powder was dispersed in ethanol followed by an ultrasonic bath treatment for 5 minutes. A drop of the suspension was applied to a lacey carbon grid (Cu150P from Okenshoji Co., Ltd). The grid was then dried in air for 10 minutes and the sample holder with the grid was transferred to a TEM.

2.2. Experimental setup

The cRED experiments have been performed on a Themis Z microscope equipped with a Gatan OneView camera (4096×4096 pixels, pixelsize: $15 \mu\text{m}$). The OneView camera is well suited for cRED data acquisition, because it has essentially no readout deadtime when in the movie mode. *In-situ* data capture mode with 1024×1024 pixels resolution (binning $\times 4$) was employed. cRED data were collected using a single-tilt TFS holder ($\pm 40^\circ$), without using a beam stopper. Since Themis Z is very stable both electrically and mechanically, a crystal tracking procedure described by (Cichocka *et al.*, 2018) is not a prerequisite for keeping the crystal centered in the beam or selected area (SA) aperture. Before data acquisition, a standard TEM alignment routine was performed. All experiments were performed in the parallel illumination mode using a $50 \mu\text{m}$ C2 condenser aperture. The Z-height of the crystal was adjusted to the eucentric height in order to minimize its movement during tilting. Diffraction patterns were focused to obtain sharp spots in the diffraction mode. The exposure time was set up to be 0.3 s per diffraction frame, the rotation speed was $1.44^\circ/\text{s}$. cRED dataset with a total rotation range of 80° contains 185 frames, collected in approximately 55 s.

For JEM 2100F equipped with a Gatan Orius SC200D detector (2048×2048 pixels, pixelsize: $7.4 \mu\text{m}$) the exposure time and rotation speed were set up to be 0.5 s/frame and $0.444^\circ/\text{s}$, resulting in 209 frames within the total rotation range of 46.42° in 104.5 s.

Two different beam settings available on Themis Z were tested, further on referred to as selected area diffraction (SAED) and nanoprobe (NP) modes. In the SAED mode, a $40 \mu\text{m}$ SA aperture was inserted to limit the area used for diffraction, whereas in the NP mode the field of view was restricted by the beam size. Spot size 5 or 6 was usually used in the SAED mode, and spot size 11 in the NP mode. The electron dose on the specimen was controlled varying the monochromator focus.

2.3. Data processing and structure determination

Diffraction images were collected in .TIFF format and converted to SMV format (.img) using the *process_DM* python script (Smeets, 2019). The collected frames were processed with the *XDS* software (Kabsch, 2010) for the spot-finding, indexing, space-group assignment, data integration, scaling, and refinement. Previously determined lattice parameters and the space group (Olson *et al.*, 1981) were used as an input, REFLECTING_RANGE_E.S.D. parameter in the XDS.INP file was set up to be 0.7 to include very sharp diffraction spots in the indexing procedure. Data statistics indicators provided in the output CORRECT.LP file were used further for data quality comparison. The reflection file for structure solution and refinement was obtained by merging several individual datasets from different crystals using the *XSCALE* sub-program. The structure was solved by *Sir2014* (Burla *et al.*, 2015) and *SHELXT* (Sheldrick, 2008) and refined by *SHELXL* using electron atomic structure factors with the help of *Olex2* software (Dolomanov *et al.*, 2009).

3. *InsteaDMatic* workflow

InsteaDMatic follows the data collection workflow described in (Cichocka *et al.*, 2018) using the continuous rotation method for electron diffraction (Arndt & Wonacott, 1977; Nederlof *et al.*, 2013; Nannenga *et al.*, 2014; Gemmi *et al.*, 2015). The same workflow has previously been implemented in Python in the program *Instamatic* (Smeets *et al.*, 2018). However, *Instamatic* requires significant development to interface both the TEM and the camera APIs.

On the camera computer, *InsteaDMatic* is run from DM and the GUI is shown in **Error! Reference source not found.** Settings for data collection (exposure, binning, *etc.*) are controlled through the camera panel in DM. When an experiment is started by pressing the “Start” button at the very bottom of the GUI, the script enters a waiting state where it constantly polls the current α tilt value. Once a change larger than a pre-defined threshold (angle activation threshold, typically 0.2°) is detected, data acquisition is initiated. The threshold also serves to eliminate any existing backlash in the α tilt direction. Rotation can then be initiated through any means available, either using the knobs, through the TEM user interface, or software.

It is worth to mention that at present the DM API does not allow fine control over the rotation speed of the goniometer although this function is available on our microscope (Themis Z, TFS) through the TEMScripting interface, as well as other recent TFS/JEOL microscopes. To be able to control the rotation through DM, we implemented a custom Python script in *Instamatic* (Smeets, 2018) to synchronize rotation with data acquisition. The script establishes an interface with the TEM on the microscope computer and accepts connections over the network. A socket interface is then established using the program ‘netcat’ (<https://nmap.org/ncat/>) on the camera computer through the DM function *LaunchExternalProcess*, which then communicates the requested rotation range and speed over the network to the microscope computer.

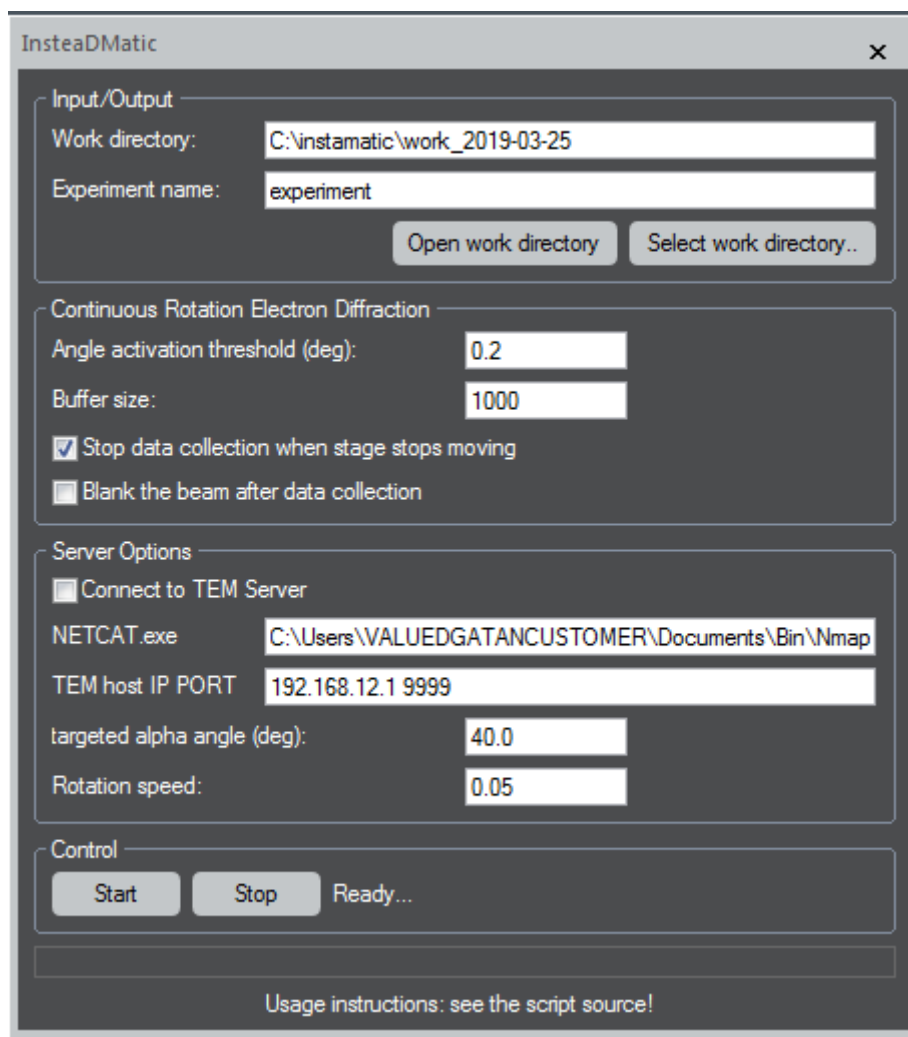


Figure 1 The graphic interface of *InsteaDMatic*.

Once rotation has been detected, data acquisition is initiated. The DM script hooks into the live view of the OneView camera, and then constantly copies the front-most image to a pre-allocated “image buffer” whose size can be defined in the GUI of the script (“buffer size”) and corresponds to the maximum number of frames that are expected to be collected. Whenever the live view is updated, DM fires an event called *DataValueChangedEvent*, which signals the script to copy the frame. The exposure time and binning are therefore defined through the DM interface, and not through the script. Data collection may be interrupted at any time by pressing the “Stop” button. There is also an automatic check for the completion of data collection, by looking at the change of α tilt after every image cloning operation. When the change is equal to 0, the data collection loop breaks automatically. Finally, the script stores all relevant experimental metadata required for processing to a new directory, such as the rotation range, exposure time, camera length, etc. The image files are stored in the same directory in TIFF format, and can be converted to other desired formats (SMV and MRC) by running the *process_DM.py* script (Smeets, 2019). A flowchart of the workflow is shown in Figure 2. Detailed

instruction of usage can be found from the script. The script is compatible with DM version 2.0 (which introduced the *DataValueChangedEvent*) or newer, and can be used with any Gatan camera that supports a streaming live view.

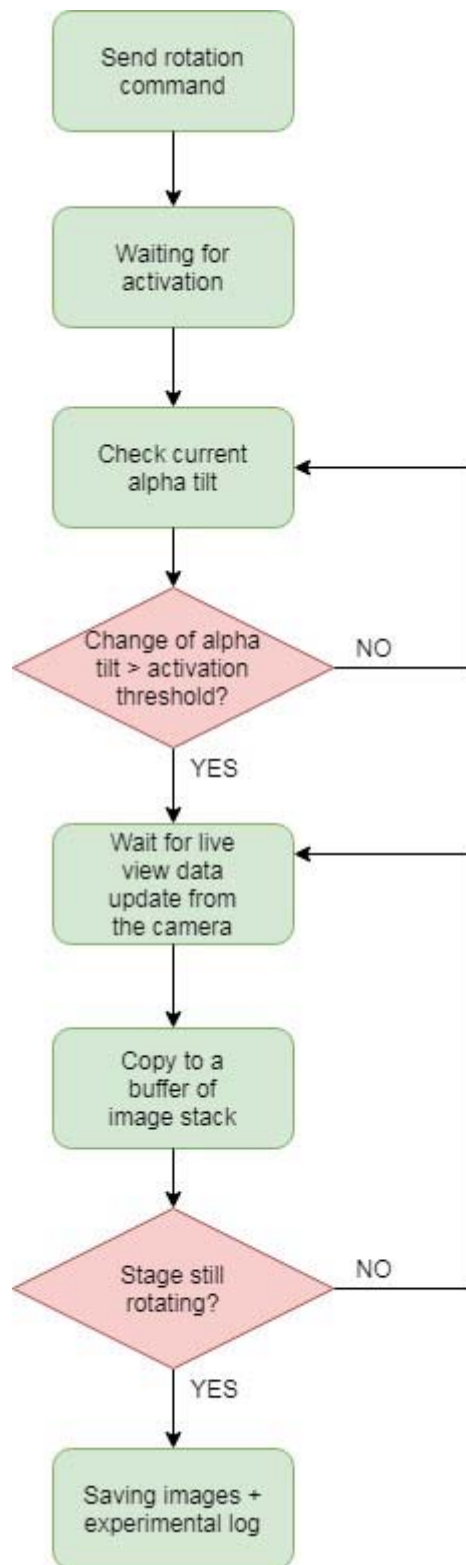


Figure 2 Flowchart of *InsteaDMatic*.

4. Application for structure determination of ZSM-5

A proof-of-concept has been performed through employing *InsteaDMatic* for data collection and further structure determination of a ZSM-5 aluminosilicate zeolite widely used in industry as a catalyst (Ji *et al.*, 2017; Kunwar *et al.*, 2016). ZSM-5 is relatively stable against beam damage, allowing multiply data to be collected from the same crystal. Consequently, a direct comparison of cRED data quality at different illumination settings becomes possible.

First, we tested *InsteaDMatic* on Themis Z with a Gatan One View CCD camera. A typical experiment was filmed in order to illustrate the procedure of cRED data acquisition, see Supporting Movie 1. The best Themis Z dataset demonstrated the completeness of more than 75% in the resolution shells ranging from 2.36 Å to 0.8 Å and R_{meas} of 13.7% (see Table S1) enabling *ab initio* crystal structure solution from this one individual dataset. Unfortunately, the completeness of most individual datasets does not exceed 50% for the orthorhombic structure, and often only merged data can provide the correct structure (see below). Thus, the OneView camera was found to be well suited for experiments that require continuous read-out of the sensor. To check if the script would work on other cameras we tested it on an Orius SC200D detector installed on JEM 2100F. A “single-crystal” dataset collected over a rotation range of 46.42° reached the completeness of ~30% in the resolution shells from 2.36 Å to 0.8 Å, and exhibited the R_{meas} of 26.1%. Although the data are of good quality, the microscope has limited tilting capabilities, and thus the low completeness of the data, prohibited a correct crystal structure solution by direct methods (*Sir2014* or *SHELXT*).

Traditionally, collection of electron diffraction data has been performed with diffraction area selection using the selected-area aperture. However, area selection can also be accomplished by adjusting the illumination settings. Almost parallel illumination with sub-micron beam diameter can be obtained either by Köhler illumination (Wu *et al.*, 2004; Meyer *et al.*, 2006; Benner *et al.*, 2011), or by inserting a small 10 µm C2 condenser aperture (Kolb *et al.*, 2007; Dwyer *et al.*, 2007). Nanoprobe gives full control on the beam diameter used and in principle also allows collecting data on a smaller area with respect to SAED (Gemmi *et al.*, 2019). However, it is worth paying attention to the direct comparison of data quality collected on the same sample by cRED in SAED and NP modes, which is currently not available from the literature. Here, an attempt has been made to reveal the difference between these modes using the same area of the sample for collecting diffraction data. In the SAED mode the beam was spread to be roughly 6 µm in diameter at 13 kX magnification and a diffraction field of about 750 nm was selected by inserting the SA. In the NP mode the beam was condensed to illuminate the 750 nm area, and the electron dose rate was kept equal to those in the SAED mode (0.05 e/Å²s) by adjusting the monochromator focus. Two resulting datasets registered on the same isolated crystal are present in Table 1.

Table 1 Data collection parameters and data processing by XDS. Statistics in different resolution shells is given in Tables S2-S3.

	SAED dataset	NP dataset
Spot size	5	11
Dose rate, $e/\text{\AA}^2\text{s}$	0.05	0.05
Diffraction area, nm	750	750
Tilt range, $^\circ$	39.64 to -40.00	-39.71 to 40.00
Oscillation angle, $^\circ$	0.430	0.429
Exposure time, s	0.30	0.30
Acquisition time per frame, s	0.30	0.30
Camera length, mm	580	580
Mono focus	100.34	78.89
Rotation speed, $^\circ/\text{s}$	1.441	1.434
Total No. of reflections	17224	17825
No. of unique reflections	2622	2692
Completeness, %	47.1	48.3
Resolution cutoff, \AA	0.80	0.80
I/σ	4.19	4.42
R_{obs} , %	20.8	21.7
R_{exp} , %	23.9	24.8
R_{meas} , %	22.8	23.9
$CC_{1/2}$	98.7	98.1
Unit cell parameters		
$a/\text{\AA}$	20.38	20.56
$b/\text{\AA}$	19.58	19.60
$c/\text{\AA}$	13.21	13.18

Based on the previous crystallographic reports about the ZSM-5 crystal structure (Olson *et al.*, 1981; van Koningsveld *et al.*, 1987), the lattice parameters $a = 20.07 \text{ \AA}$, $b = 19.92 \text{ \AA}$, $c = 13.42 \text{ \AA}$ and the space group $Pnma$ (#62) were used as an input for XDS. Both SAED and NP datasets fit well with the expected orthorhombic structure and the refined unit cell parameters are close to the published values within the accuracy of the electron diffraction method. Figure 3 shows the reconstructed reciprocal lattice of ZSM-5 based on the cRED data collected in the SAED mode, from Table 1.

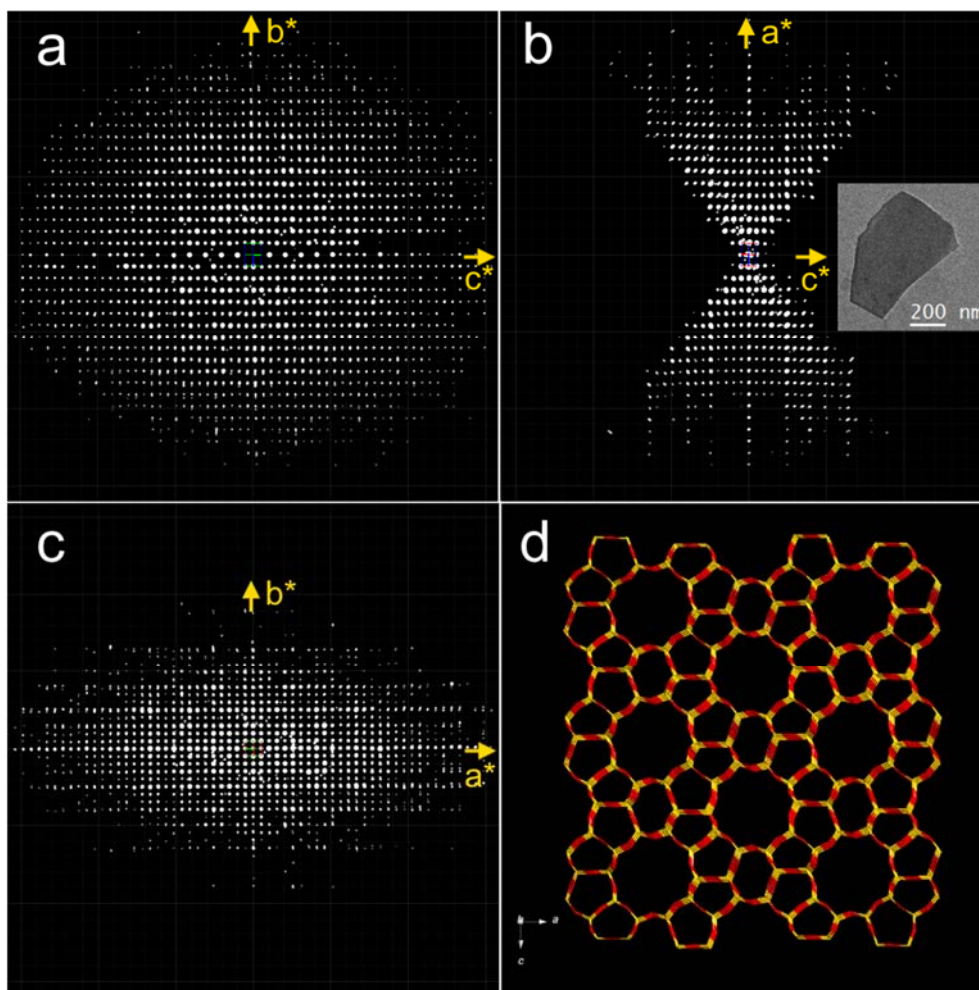


Figure 3 (a-c) Typical 3D reciprocal lattice of ZSM-5 reconstructed and visualized by *REDp* (Wan *et al.*, 2013). The corresponding crystal image is shown as an inset in (b). (d) The wires/sticks ZSM-5 crystal structure representation.

Among factors affecting the cRED data quality electron dose has an utmost importance. Our experiments have been show that the optimal electron dose rate range for ZSM-5 data acquisition is between $0.05 \text{ e}/\text{\AA}^2\text{s}$ and $0.1 \text{ e}/\text{\AA}^2\text{s}$ (Figure 4). In the optimal range, higher the dose the better I/σ , however we observed that I/σ for NP datasets is systematically slightly higher than for SAED ones, especially for the low-resolution data. Excessive electron dose ($>0.2 \text{ e}/\text{\AA}^2\text{s}$) causes read-out biases of the OneView camera, whereas low electron dose rate $<0.03 \text{ e}/\text{\AA}^2\text{s}$ leads to significant deterioration of the signal-noise ratio and, as a consequence, to poor data statistics. Some of the raw SAED/NP diffraction patterns collected at different electron doses are shown in Figure S1.

It should be mentioned that unlike low-d Bragg peaks which can easily be discriminated from a slowly-varying background in diffraction patterns, the high-d peaks are often not very intense and thus cannot be readily separated from the background. Since XDS is relying upon the smallest

measured intensities to guide the subtraction of the background, the scaling of the Bragg intensities as a function of resolution shells unavoidably leads to significant deteriorations of weak but still useful high-resolution signal, and consequently, to higher R-values in the 1.00 – 0.80 Å resolution shells. For X-ray diffraction a common practice would be a truncating data at the resolution at which R_{meas} remains below ~60% and $\langle I/\sigma \rangle$ is ~2 or higher. However, for electron diffraction, we found that including data out to a $CC_{1/2}$ value (Karplus & Diederichs, 2015) of ~70% lead to an improvement of the refined model even though the data at that resolution have $R_{\text{meas}} \sim 200 - 300\%$.

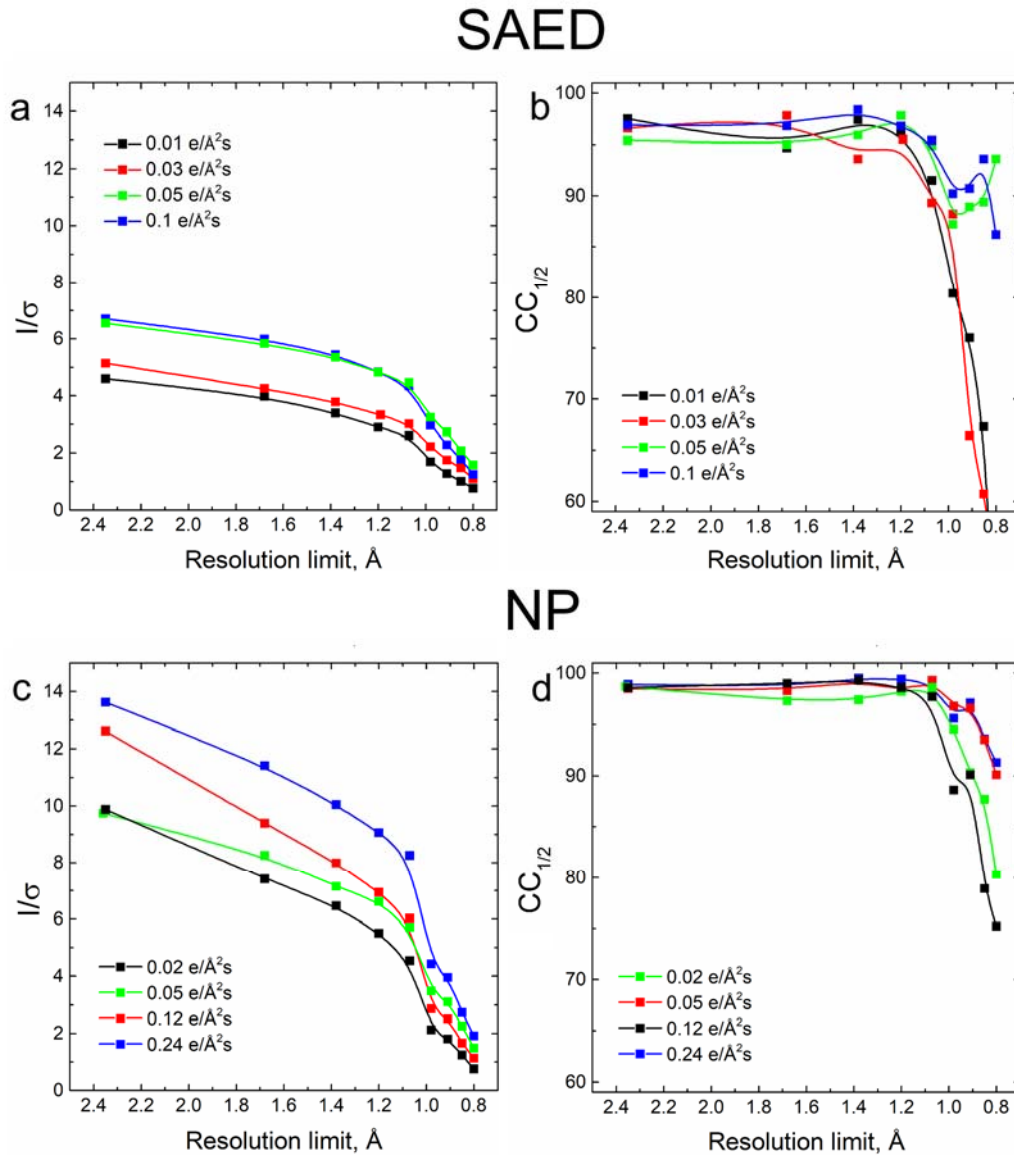


Figure 4 (a-b) Statistics of the cRED diffraction data collected in SAED and (c-d) NP modes for different electron doses: I/σ and $CC_{1/2}$ against the resolution. All SAED data were collected from the same ZSM-5 crystal sequentially, in the ascending order of the electron dose rate. NP data were collected from the second crystal following the same procedure. All lines in the figure are a guide for the eye.

Another important factor for data collection is the stability of the *CompuStage*, since preserving the same illumination field and the same scattering volume during data collection is a key factor for reliable integration of the reflection intensities. We observed only a few-nm drift of the crystal with dimensions of about 100×100 nm inside the SA aperture in the tilting range from -40 to 40° , accompanied by a ~ 50 nm jump in the beginning of rotation, see Supporting Movie 2. Thus, the *CompuStage* was found to be perfectly stable for the cRED data acquisition. However, it is worth to mention that *InsteaDMatic* does not provide an opportunity to track the crystal during the experiment, thus, at higher tilt values the crystal might move out from the SA aperture due to uncompensated Z-height changes. Specific morphology of ZSM-5 crystals having a preferred orientation together with a limited tilting range accessible by the single-tilt holder often lead to the low completeness of the individual dataset. Therefore, it is necessary to merge data from several crystallites for a relevant structure solution. Partially this problem can be overcome by using a high-tilt tomography holder, with accessible tilt range $\pm 80^\circ$, but the possible instability of the goniometer at high tilt angles should be always taken into account.

For the structure solution, five individual SAED datasets collected from different crystals were merged, chosen by performing hierarchical cluster analysis based on 15 experiments. Hierarchical cluster analysis helps to find structurally similar data with high correlation coefficients between scaled diffraction intensities and to reach high completeness by merging only few datasets (Wang *et al.*, 2019). *Sir2014* (Burla *et al.*, 2015) direct space and *SHELXT* dual space methods (Sheldrick, 2008) can be both employed for the structure solution. We noted that a minimal signal-to-noise ratio of about 2 (in 1.0 \AA resolution limit) is required for revealing the framework of ZSM-5 by means of direct methods, whereas dual space methods are not so sensitive to the I/σ ratio. The atomic positions of all 12 Si- and 24 O-atoms have been successfully found and used as an initial structural model. After the refinement, the model converged with $R_1=0.1998$ and $GOF=1.59$ (Table 2). All Si and O atoms were refined anisotropically (Figure 5) following by applying the rigid-body restraint (RIGU command (Thorn *et al.*, 2012)). No additional restraints on Si-O bond lengths and O-Si-O angles have been applied. The three-dimensional channel system of ZSM-5 consists of straight channels running parallel to $[010]$ having 10-rings of ca. $5.4 \times 5.6 \text{ \AA}$ diameter and sinusoidal channels running parallel to $[100]$ having 10-ring openings of ca. $5.1 \times 5.4 \text{ \AA}$, in full agreement with the previous XRD data (Olson *et al.*, 1981; van Koningsveld *et al.*, 1987).

The refined SAED model was compared with the reference ZSM-5 crystal structure (van Koningsveld *et al.*, 1987) obtained from XRD data using COMPSTRU program (Flor *et al.*, 2016). The average displacement between the corresponding Si atoms found to be $0.04(2) \text{ \AA}$, whereas between O atoms the value is $0.06(4) \text{ \AA}$. All deviations of atomic positions between the reference ZSM-5 structure (van Koningsveld *et al.*, 1987) and those determined from cRED data are listed in Table S6. It is

interesting to compare the accuracy of the atomic positions determination for ZSM-5 with the data collected on a widely used JEM-2100 LaB₆ microscope (Wang, Yang *et al.*, 2018). An average deviation from the same reference structure (van Koningsveld *et al.*, 1987) of about 0.07(4) Å was reported, however, DFIX restraints were applied to Si—O distances (1.61 Å) (Wang, Yang *et al.*, 2018). In our case a better accuracy is achieved with no additional geometry restraints.

Table 2 Selected crystallographic data for merged ZSM-5 datasets. Space group *Pnma* (#62), *Z* = 1, wavelength λ = 0.019 Å. Statistics in different resolution shells is given in Tables S4-S5

	SAED	NP
Datasets merged	5	6
Averaged unit cell parameters		
<i>a</i> /Å	20.19	20.10
<i>b</i> /Å	19.56	19.47
<i>c</i> /Å	12.95	13.30
Total No. of reflections	61596	65672
No. of unique reflections	5159	5299
No. of reflections with $I > 2\sigma(I)$	2854	3903
Completeness, %	95.8	98.2
Resolution cutoff, Å	0.80	0.80
<i>I</i> / σ	3.56	4.56
<i>R</i> _{obs} , %	33.0	24.0
<i>R</i> _{exp} , %	33.8	27.7
<i>R</i> _{meas} , %	34.9	25.2
<i>CC</i> _{1/2}	94.8	97.4
<i>R</i> ₁ ($I > 2\sigma(I)$)	0.1998	0.1764
w <i>R</i> ₂ ($I > 2\sigma(I)$)	0.2625	0.2004
<i>R</i> ₁ (all data)	0.5109	0.4760
w <i>R</i> ₂ (all data)	0.5490	0.4928
GOF	1.59	1.61

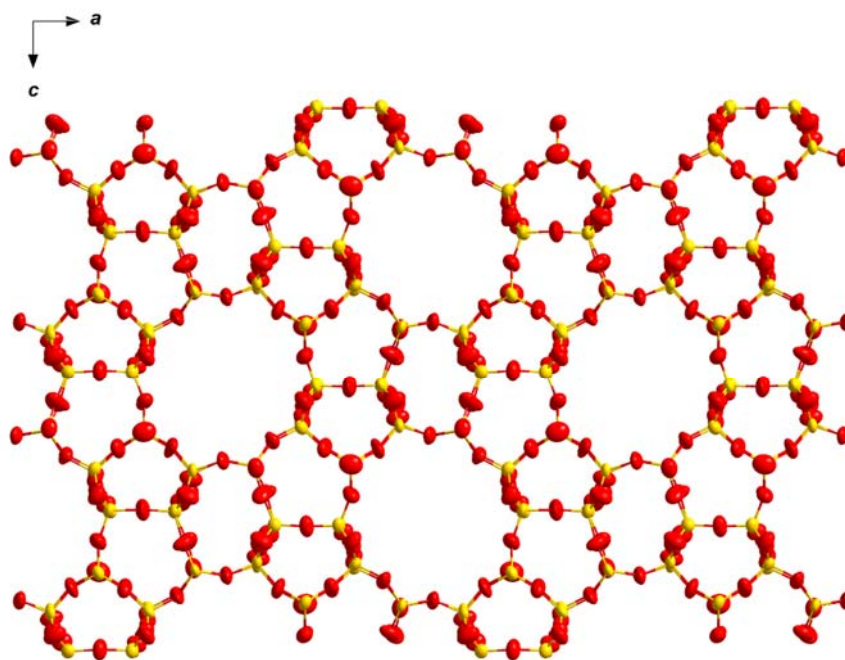


Figure 5 Refined structure of ZSM-5 viewed along b -axis showing anisotropic atomic displacement parameters for Si (yellow) and O (red) atoms.

The nanoprobe mode provides more flexibility in adjustment of the diffraction field diameter, which can be precisely fitted for each individual crystallite, in contrast to the SAED mode, which is limited by pre-defined aperture sizes. It should be also mentioned that in NP, when the illumination system is close to switching or has switched to condensing mode, the beam converges significantly faster as at standard settings causing some difficulties with the focus of diffraction patterns. NP datasets usually demonstrate higher signal-to-noise ratio as compared to the SAED data, whereas other crystallographic indicators are virtually of the same order (Table 1). The structure was solved from six merged NP datasets chosen from 10 datasets by means of hierarchical cluster analysis, and refined anisotropically to $R_1=0.1764$ and $GOF=1.61$ (Table 2). A comparison with the reference model (van Koningsveld *et al.*, 1987) shows that the average displacements between the corresponding atoms are even lower than those for the SAED model (Table S6). The estimated average displacements between Si atoms is $0.03(1)$ Å, between O atoms – $0.05(3)$ Å, arguing for somewhat better data quality of the merged NP dataset.

Summarizing our findings, the selection of diffraction field by illumination provides reliable results comparable with the traditional SAED method and may be highly beneficial for studies of beam sensitive materials since it paves an avenue for tailoring of the electron dose received by a specimen in a controllable manner.

5. Conclusion

A new custom DigitalMicrograph script named *InsteaDMatic* has been developed to facilitate rapid automated electron diffraction data acquisition. *InsteaDMatic* was successfully examined on both JEOL and Thermo Fisher Scientific microscopes that utilize Gatan DigitalMicrograph for control over the instrument. The script was employed for data collection and structural determination of ZSM-5 zeolite framework. Dose rate between $0.05 \text{ e}/\text{\AA}^2\text{s}$ and $0.10 \text{ e}/\text{\AA}^2\text{s}$ found to be optimal for obtaining high quality data with up to 0.80 \AA resolution. Positions of the Si and O atoms in ZSM-5 can be found within an accuracy better than 0.06 \AA , compared to those obtained by single-crystal XRD data. Both SAED and Nanoprobe beam settings deliver reliable high quality structural data, provided that the beam and CompuStage are stable during the goniometer rotation. Varying the monochromator focus offer an additional degree of freedom for tailoring the electron dose, which is especially relevant in the Nanoprobe mode. We anticipate that the present research will contribute to the development of widely applicable routine for the structure determination of micro- and nanocrystals by cRED.

The *InsteaDMatic* script described in this article available from.

<https://github.com/stefsmeets/InsteaDMatic>

Acknowledgements We would like to acknowledge electron microscopy groups of NTNU, Norway, Sun Yat-sen University (SYSU), China, and Peking University, Shenzhen campus, China for their interest in the testing of *InsteaDMatic*.

References

- Arndt, U. W. & Wonacott, A. J. (1977). *Rotation method in crystallography* North-Holland Pub. Co.
- Benner, G., Niebel, H. & Pavia, G. (2011). *Crystal Research and Technology*. **46**, 580–588.
- Bieseki, L., Simancas, R., Jordá, J., Bereciartua, P., Cantín, Á., Simancas, J., B. Pergher, S., Valencia, S., Rey, F. & Corma, A. (2018). *Chemical Communications*. **54**, 2122–2125.
- Brázda, P., Palatinus, L. & Babor, M. (2019). *Science*. **364**, 667–669.
- Burla, M. C., Caliandro, R., Carrozzini, B., Cascarano, G. L., Cuocci, C., Giacovazzo, C., Mallamo, M., Mazzone, A. & Polidori, G. (2015). *J Appl Cryst.* **48**, 306–309.
- Cichocka, M. O., Ångström, J., Wang, B., Zou, X. & Smeets, S. (2018). *J Appl Cryst.* **51**, 1652–1661.
- de la Cruz, M. J., Hattne, J., Shi, D., Seidler, P., Rodriguez, J., Reyes, F. E., Sawaya, M. R., Cascio, D., Weiss, S. C., Kim, S. K., Hinck, C. S., Hinck, A. P., Calero, G., Eisenberg, D. & Gonen, T. (2017). *Nat. Methods*. **14**, 399–402.
- de la Cruz, M. J., Martynowycz, M. W., Hattne, J. & Gonen, T. (2019). *Ultramicroscopy*. **201**, 77–80.
- Denysenko, D., Grzywa, M., Tonigold, M., Streppel, B., Krkljus, I., Hirscher, M., Mugnaioli, E., Kolb, U., Hanss, J. & Volkmer, D. (2011). *Chemistry – A European Journal*. **17**, 1837–1848.
- Dolomanov, O. V., Bourhis, L. J., Gildea, R. J., Howard, J. a. K. & Puschmann, H. (2009). *J Appl Cryst.* **42**, 339–341.
- Dwyer, C., Kirkland, A. I., Hartel, P., Müller, H. & Haider, M. (2007). *Appl. Phys. Lett.* **90**, 151104.
- Feyand, M., Mugnaioli, E., Vermoortele, F., Bueken, B., Dieterich, J. M., Reimer, T., Kolb, U., de Vos, D. & Stock, N. (2012). *Angewandte Chemie International Edition*. **51**, 10373–10376.
- Flor, G. de la, Orobengoa, D., Tasci, E., Perez-Mato, J. M. & Aroyo, M. I. (2016). *J Appl Cryst.* **49**, 653–664.
- Gemmi, M., La Placa, M. G. I., Galanis, A. S., Rauch, E. F. & Nicolopoulos, S. (2015). *J Appl Cryst.* **48**, 718–727.
- Gemmi, M., Mugnaioli, E., Gorelik, T. E., Kolb, U., Palatinus, L., Boullay, P., Hovmöller, S. & Abrahams, J. P. (2019). *ACS Cent. Sci.*
- van Genderen, E., Clabbers, M. T. B., Das, P. P., Stewart, A., Nederlof, I., Barentsen, K. C., Portillo, Q., Pannu, N. S., Nicolopoulos, S., Gruene, T. & Abrahams, J. P. (2018). *Acta Crystallogr. Sect. A*. **74**, 709–709.

-
- Guo, P., Shin, J., Greenaway, A. G., Min, J. G., Su, J., Choi, H. J., Liu, L., Cox, P. A., Hong, S. B., Wright, P. A. & Zou, X. (2015). *Nature*. **524**, 74–78.
- Ji, Y., Yang, H. & Yan, W. (2017). *Catalysts*. **7**, 367.
- Jiang, J., Jorda, J. L., Yu, J., Baumes, L. A., Mugnaioli, E., Diaz-Cabanas, M. J., Kolb, U. & Corma, A. (2011). *Science*. **333**, 1131–1134.
- Kabsch, W. (2010). *Acta Cryst D*. **66**, 125–132.
- Karplus, P. A. & Diederichs, K. (2015). *Curr Opin Struct Biol*. **34**, 60–68.
- Kolb, U., Gorelik, T., Kübel, C., Otten, M. T. & Hubert, D. (2007). *Ultramicroscopy*. **107**, 507–513.
- van Koningsveld, H., van Bekkum, H. & Jansen, J. C. (1987). *Acta Cryst B*. **43**, 127–132.
- Kunwar, B., Cheng, H. N., Chandrashekar, S. R. & Sharma, B. K. (2016). *Renewable and Sustainable Energy Reviews*. **54**, 421–428.
- Lee, H., Shin, J., Choi, W., Choi, H. J., Yang, T., Zou, X. & Hong, S. B. (2018). *Chem. Mater*. **30**, 6619–6623.
- Lenzen, D., Zhao, J., Ernst, S.-J., Wahiduzzaman, M., Inge, A. K., Fröhlich, D., Xu, H., Bart, H.-J., Janiak, C., Henninger, S., Maurin, G., Zou, X. & Stock, N. (2019). *Nature Communications*. **10**, 3025.
- Meyer, J. C., Paillet, M., Duesberg, G. S. & Roth, S. (2006). *Ultramicroscopy*. **106**, 176–190.
- Nannenga, B. L., Shi, D., Leslie, A. G. W. & Gonen, T. (2014). *Nature Methods*. **11**, 927–930.
- Nederlof, I., van Genderen, E., Li, Y.-W. & Abrahams, J. P. (2013). *Acta Cryst D*. **69**, 1223–1230.
- Olson, D. H., Kokotailo, G. T., Lawton, S. L. & Meier, W. M. (1981). *J. Phys. Chem*. **85**, 2238–2243.
- Sheldrick, G. M. (2008). *Acta Crystallogr. Sect. A*. **64**, 112–122.
- Simancas, J., Simancas, R., Bereciartua, P. J., Jorda, J. L., Rey, F., Corma, A., Nicolopoulos, S., Pratim Das, P., Gemmi, M. & Mugnaioli, E. (2016). *J. Am. Chem. Soc*. **138**, 10116–10119.
- Smeets, S. (2018). Instamatic, a Python program to collect serial and rotation electron diffraction data. Source code available from <https://github.com/stefsmeeets/instamatic>.
- Smeets, S. (2019). Process_DM.py script. Source code available from https://github.com/stefsmeeets/instamatic/blob/master/scripts/process_dm.py.
- Smeets, S., Wang, B., Cichocka, M. O., Ångström, J. & Wan, W. (2018). Instamatic Zenodo.

-
- Thorn, A., Dittrich, B. & Sheldrick, G. M. (2012). *Acta Cryst A*. **68**, 448–451.
- Wan, W., Sun, J., Su, J., Hovmoller, S. & Zou, X. (2013). *J. Appl. Crystallogr.* **46**, 1863–1873.
- Wang, B., Rhauderwiek, T., Inge, A. K., Xu, H., Yang, T., Huang, Z., Stock, N. & Zou, X. (2018). *Chemistry – A European Journal*. **24**, 17429–17433.
- Wang, B., Zou, X. & Smeets, S. (2019). *IUCrJ*. **6**, 854–867.
- Wang, Y., Yang, T., Xu, H., Zou, X. & Wan, W. (2018). *J Appl Cryst.* **51**, 1094–1101.
- Wu, J. S., Melcer, N., Sharp, W. P., O’Keeffe, M., Spence, J. C. H. & Yaghi, O. M. (2004). *Ultramicroscopy*. **98**, 145–150.
- Xu, H., Lebrette, H., Clabbers, M. T. B., Zhao, J., Griese, J. J., Zou, X. & Högbom, M. (2019). *Science Advances*. **5**, eaax4621.
- Zhang, C., Kapaca, E., Li, J., Liu, Y., Yi, X., Zheng, A., Zou, X., Jiang, J. & Yu, J. (2018). *Angewandte Chemie International Edition*. **57**, 6486–6490.
- Zhang, D., Oleynikov, P., Hovmöller, S. & Zou, X. (2010). *Zeitschrift Für Kristallographie International Journal for Structural, Physical, and Chemical Aspects of Crystalline Materials*. **225**, 94–102.

Supporting information

Table S1 Comparison of cRED data from Themis Z with One View camera and JEM2100F with Orius SC200D camera.

	Themis Z / One View	JEOL2100F / Orius SC200D
Spot size	5	1
Dose rate, e/Å ² s	0.05	0.084
Diffraction area, nm	750	1200
Tilt range, °	29.77 to -29.99	-22.48 to 23.94
Oscillation angle, °	0.424	0.222
Exposure time, s	0.30	0.50
Acquisition time per frame, s	0.30	0.50
Camera length, mm	580	800
Rotation speed, °/s	1.421	0.444
Rotation axis, °	-171	-42.5
Total No. of reflections	12058	11042
No. of unique reflections	4276	2086
Completeness, %	77.7	34.5
Resolution cutoff, Å	0.80	0.80
I/σ	4.19	3.08
R_{obs} , %	11.0	23.3
R_{exp} , %	12.4	30.0
R_{meas} , %	13.7	26.1
$CC_{1/2}$	98.9	98.6
Unit cell parameters		
a/Å	19.93	20.68
b/Å	19.48	20.49
c/Å	13.46	13.75

Table S2 Statistics of an individual cRED dataset collected in SAED mode on Themis Z in different resolution shells.

Resolution limit	#obs	#uniq	#pos	comp, %	R_{obs} , %	R_{exp} , %	#comp	I/σ	R_{meas} , %	$CC_{1/2}$
2.35	605	107	233	45.9	12.2	13.2	601	10.91	13.5	98.3
1.68	1101	181	382	47.4	16.0	14.9	1097	8.24	17.6	98.0
1.38	1460	233	496	47.0	17.0	16.0	1452	7.41	18.7	98.5
1.20	1789	276	574	48.1	19.2	19.1	1785	6.27	21.2	97.9
1.07	2103	312	650	48.0	21.8	22.0	2098	5.47	23.7	97.9
0.98	2315	344	719	47.8	43.8	52.1	2300	3.09	47.6	93.9
0.91	2502	374	786	47.6	48.0	72.4	2489	2.51	52.2	92.5
0.85	2724	400	832	48.1	70.5	117.0	2714	1.71	76.5	90.1
0.80	2625	395	890	44.4	89.3	173.9	2614	1.21	97.0	88.7
total	17224	2622	5562	47.1	20.8	23.9	17150	4.19	22.8	98.5

Table S3 Statistics of an individual cRED dataset collected in Nanoprobe mode on Themis Z in different resolution shells.

Resolutio n limit	#obs	#uniq	#pos	comp , %	R_{obs} , %	R_{exp} , %	#comp	I/σ	R_{meas} , %	$CC_{1/2}$
2.36	653	112	234	47.9	13.2	15.6	651	9.74	14.6	98.7
1.68	1149	182	384	47.4	17.5	16.8	1146	8.26	19.2	97.3
1.38	1500	239	490	48.8	21.4	18.3	1495	7.15	23.5	95.4
1.20	1845	275	578	47.6	22.4	21.0	1843	6.61	24.8	98.2
1.07	2092	319	649	49.2	23.0	22.9	2079	5.71	25.1	98.6
0.98	2382	351	721	48.7	40.9	55.0	2376	3.48	44.8	94.5
0.91	2600	380	789	48.2	44.8	69.2	2595	3.10	49.1	90.3
0.85	2782	409	829	49.3	57.6	101.3	2767	2.25	62.9	90.7
0.80	2822	425	899	47.3	65.2	144.0	2810	1.49	71.1	93.7
total	17825	2692	5573	48.3	21.7	24.8	17762	4.42	23.9	98.1

Table S4 Statistics of SAED dataset merged from 5 crystals in different resolution shells.

Resolution limit	#obs	#uniq	#pos	comp, %	R_{obs} , %	R_{exp} , %	#comp	I/σ	R_{meas} , %	$CC_{1/2}$
3.58	571	61	67	91.0	21.8	27.3	571	7.64	23.4	94.2
2.53	1051	104	110	94.5	25.4	27.1	1051	7.35	26.7	95.5
2.07	1479	143	150	95.3	29.5	27.7	1479	6.91	31.2	97.4
1.79	1796	164	175	93.7	23.7	27.7	1796	6.77	25.1	98.2
1.60	1927	179	189	94.7	32.6	28.6	1927	6.06	34.6	88.9
1.46	2228	201	208	96.6	32.7	30.5	2226	5.71	34.3	98.4
1.35	2641	233	241	96.7	34.1	29.9	2640	5.22	36.0	94.3
1.26	2755	238	244	97.5	50.8	33.7	2752	4.99	53.5	81.3
1.19	2995	256	267	95.9	34.2	33.0	2994	5.15	36.1	93.8
1.13	3165	269	277	97.1	40.7	35.2	3163	4.85	42.7	93.4
1.08	3373	278	289	96.2	48.2	43.5	3370	4.07	50.8	90.9
0.99	3883	304	318	95.6	93.8	101.8	3881	2.82	98.0	89.1
0.92	4093	327	334	97.9	113.9	131.4	4089	2.45	119.2	86.6
0.89	4500	350	366	95.6	134.7	160.6	4498	2.30	140.6	86.2
0.84	4823	371	380	97.6	251.8	337.5	4819	1.74	262.5	61.4
0.82	4732	366	381	96.1	296.4	405.5	4729	1.53	309.0	55.8
0.80	3357	337	390	86.4	255.0	394.5	3347	1.35	267.6	69.2
total	61596	5159	5386	95.8	33.0	33.8	61551	3.56	34.9	94.8

Table S5 Statistics of Nanoprobe dataset merged from 6 crystals in different resolution shells.

Resolution limit	#obs	#uniq	#pos	comp, %	R_{obs} , %	R_{exp} , %	#comp	I/σ	R_{meas} , %	$CC_{1/2}$
3.58	705	67	68	98.5	20.0	23.6	705	9.53	21.2	98.0
2.53	1302	112	112	100.0	17.0	24.0	1302	9.00	17.9	98.5
2.07	1775	146	146	100.0	19.6	24.5	1775	8.59	20.6	97.7
1.79	2188	175	175	100.0	22.3	24.8	2188	7.81	23.6	97.5
1.60	2507	196	196	100.0	21.4	25.9	2507	7.44	22.5	98.5
1.46	2690	203	205	99.0	29.8	27.4	2690	6.98	31.2	99.6
1.35	3066	232	233	99.6	23.4	26.5	3066	6.84	24.6	84.3
1.27	3422	255	255	100.0	28.2	29.5	3422	6.13	29.5	98.9
1.19	3528	258	258	100.0	26.2	29.6	3528	6.38	27.4	98.8
1.13	3881	287	288	99.7	27.7	30.7	3881	5.83	28.9	96.6
1.08	4016	283	285	99.3	38.8	39.1	4016	5.22	40.4	98.8
0.99	3804	324	325	99.7	53.3	51.6	3804	3.73	55.9	95.3
0.92	4069	341	341	100.0	54.4	56.9	4069	3.41	57.1	92.7
0.89	4268	358	358	100.0	67.0	65.6	4268	2.89	70.1	92.3
0.84	4731	395	395	100.0	90.4	103.9	4731	2.27	94.7	84.3
0.82	4490	383	388	98.7	91.6	114.8	4490	2.18	95.9	95.7
0.80	3234	310	394	78.7	91.8	112.8	3227	1.83	96.6	83.7
total	65672	5299	5397	98.2	24.0	27.7	65665	4.56	25.2	97.4

Table S6 Deviations of atomic positions between the reference ZSM-5 structure (van Koningsveld *et al.*, 1987) and those determined from cRED data collected in SAED/NP modes. Fractional atomic coordinates for the reference ZSM-5 structure are given in Table S7. The origin shift between reference and refined structures can be expressed by a transformation matrix (P, p): a,b,c ; $1/2,0,1/2$.

Atom label	Atomic displacement SAED, Å	Atomic displacement NP, Å
Si1	0.0467	0.0295
Si2	0.0859	0.0474
Si3	0.0373	0.0243
Si4	0.0294	0.0242
Si5	0.0146	0.0234
Si6	0.0521	0.0153
Si7	0.0230	0.0076
Si8	0.0394	0.0265
Si9	0.0413	0.0429
Si10	0.0552	0.0509
Si11	0.0492	0.0316
Si12	0.0541	0.0144
O1	0.0735	0.0970
O2	0.1003	0.0350
O3	0.0134	0.0247
O4	0.0581	0.0509
O5	0.0307	0.0222
O6	0.0423	0.0289
O7	0.0515	0.0333
O8	0.0430	0.0329
O9	0.0166	0.0464
O10	0.1547	0.0933
O11	0.0413	0.0391
O12	0.1019	0.1142
O13	0.1135	0.1111
O14	0.1061	0.0297
O15	0.0427	0.0570
O16	0.0305	0.0190
O17	0.0564	0.0364
O18	0.0486	0.0754

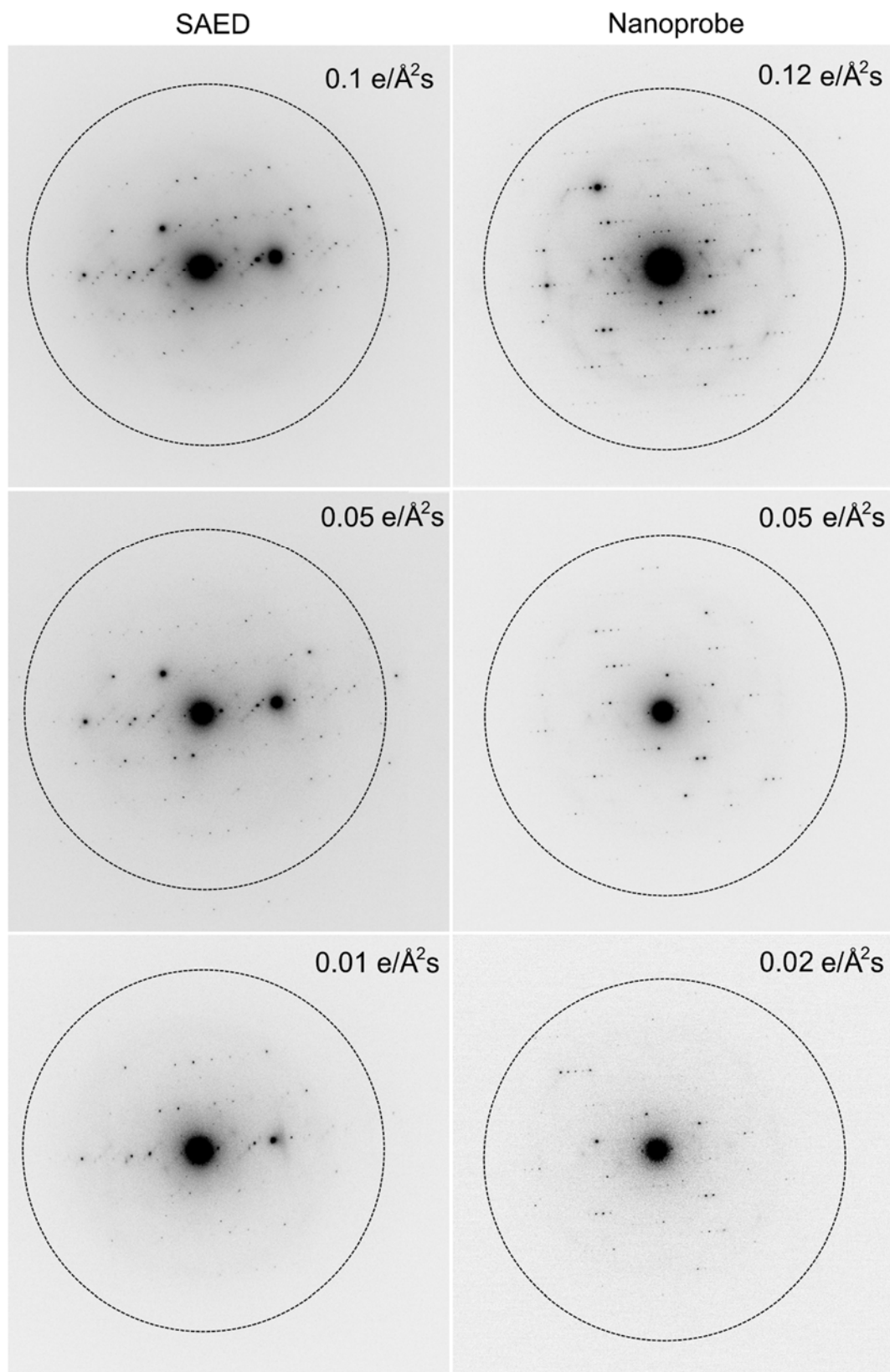
O19	0.0402	0.0556
O20	0.0186	0.0180
O21	0.0576	0.0368
O22	0.0441	0.0830
O23	0.0816	0.0957
O24	0.0432	0.0344
O25	0.0625	0.0420
O26	0.1513	0.0626
<Si> average	0.04(2)	0.03(1)
<O> average	0.06(4)	0.05(3)

Table S7 Fractional atomic coordinates for the reference ZSM-5 structure (van Koningsveld *et al.*, 1987).

	<i>x</i>	<i>y</i>	<i>z</i>
Si1	0.4224	0.0565	-0.3360
Si2	0.3072	0.0277	-0.1893
Si3	0.2791	0.0613	0.0312
Si4	0.1221	0.0630	0.0267
Si5	0.0713	0.0272	-0.1855
Si6	0.1864	0.0590	-0.3282
Si7	0.4227	-0.1725	-0.3272
Si8	0.3078	-0.1302	-0.1855
Si9	0.2755	-0.1728	0.0311
Si10	0.1206	-0.1731	0.0298
Si11	0.0704	-0.1304	-0.1820
Si12	0.1871	-0.1733	-0.3193
O1	0.3726	0.0534	-0.2442
O2	0.3084	0.0587	-0.0789
O3	0.2007	0.0592	0.0289
O4	0.0969	0.0611	-0.0856
O5	0.1149	0.0541	-0.2763
O6	0.2435	0.0553	-0.2460
O7	0.3742	-0.1561	-0.2372
O8	0.3085	-0.1552	-0.0728
O9	0.1980	-0.1554	0.0288
O10	0.0910	-0.1614	-0.0777
O11	0.1169	-0.1578	-0.2694
O12	0.2448	-0.1594	-0.2422
O13	0.3047	-0.0510	-0.1866
O14	0.0768	-0.0519	-0.1769
O15	0.4161	0.1276	-0.3896
O16	0.4086	-0.0017	-0.4136
O17	0.4020	-0.1314	-0.4239
O18	0.1886	0.1298	-0.3836
O19	0.1940	0.0007	-0.4082
O20	0.1951	-0.1291	-0.4190

O21	-0.0037	0.0502	-0.2080
O22	-0.0040	-0.1528	-0.2078
O23	0.4192	-0.2500	-0.3540
O24	0.1884	-0.2500	-0.3538
O25	0.2883	-0.2500	0.0579
O26	0.1085	-0.2500	0.0611

Figure S1 Typical diffraction patterns of ZSM-5 collected on Themis Z at different electron dose rates. Dotted rings indicate 0.8 Å resolution.



Supporting movie S1

<https://stockholmuniversity.box.com/s/96cfu9kspo4vohuzynz092o47cpj0722>

Supporting movie S2

<https://stockholmuniversity.box.com/s/f16110mb015o97d5qurdsharahpcpfzz>